RSC Advances

PAPER

View Article Online
View Journal | View Issue

Cite this: *RSC Adv.*, 2022, **12**, 1130

Efficient and selective removal of Pb(II) from aqueous solution by a thioether-functionalized lignin-based magnetic adsorbent†

Xuan Zhou,[ab] Yunlong Liu,[a] Can Jin,[*a] Guomin Wu,[a] Guifeng Liu[a] and Zhenwu Kong*[a]

The effective and selective removal of heavy metal ions from sewage is a major challenge and is of great significance to the treatment and recovery of metal waste. Herein, a novel magnetic lignin-based adsorbent L@MNP was synthesized by a thiol–ene click reaction under ultraviolet (UV) light irradiation. Multiple characterization techniques, including Fourier transform infrared (FT-IR) spectrometry, X-ray diffraction (XRD), elemental analysis, vibrating sample magnetometry (VSM), scanning electron microscopy (SEM) and transmission electron microscopy (TEM), confirmed the formed nano-morphology and structure of L@MNP. The effects of pH, contact time, initial metal concentration and temperature on the batch adsorption of Pb(II) by L@MNP were investigated. Due to the existence of sulfur and oxygen-containing sites, the maximum adsorption capacity of L@MNP for Pb(II) could reach 97.38 mg g^{-1}, while the adsorption equilibrium was achieved within 30 min. The adsorption kinetics and isotherms were well described by the pseudo-second-order model and Langmuir model, respectively, suggesting a chemical and monolayer adsorption process. In addition, L@MNP showed a high adsorption selectivity (k_{Pb} = 0.903) toward Pb(II) in the presence of other co-existing metal ions. The experimental results also revealed that L@MNP displayed structural stability, ease of recovery under an external magnetic field, and acceptable recyclability after the fifth cycle. Considering its facile preparation, low cost and high adsorption efficiency, the developed L@MNP adsorbent demonstrated great potential in removing heavy metal ions from wastewater.

Received 9th September 2021
Accepted 10th December 2021

DOI: 10.1039/d1ra06774e

rsc.li/rsc-advances

1. Introduction

Pollution of sewage containing heavy metal ions is an urgent problem facing the world,[1,2] due to their high biological toxicity and bioaccumulation. As one of the most toxic heavy metal pollutants in wastewater, lead (Pb) can easily accumulate in the human body through the food chain, causing severe damage to organs and tissues, even at low concentrations.[3,4] Humans can suffer from long-term brain damage when the Pb(II) concentration is over 50 μg L^{-1} in drinking water; therefore, the World Health Organization has stated that the allowable limit of Pb(II) content in drinking water is 10 μg L^{-1}.[5] To date, a variety of technologies for removing Pb(II) from wastewater have been developed,[6] including coagulation–flocculation, adsorption, membrane separation,[7,8] ion exchange and electrochemical precipitation.[9] The adsorption method stands out from the rest due to its economic performance, high efficiency and simple operation.[10] Despite these advantages, conventional adsorbents still need to be improved in actual application, which puts forward specific requirements for improving the recycling efficiency and avoiding secondary pollution after discarding.[11]

Magnetic adsorbents have been recently utilized in the field of wastewater purification due to their outstanding superiority of being readily removed after adsorption under an external magnetic field.[12] Normally, magnetic nanoparticles are used as magnetic cores, which can be easily coated with polymeric components to enhance their physicochemical stability and dispersion properties.[13] Although different polymers[14] such as polyacrylamide, polyacrylate and polystyrene have been introduced onto the surface of magnetic cores as shell layers for heavy metal removal, these fossil-based chemicals suffer from high energy consumption and non-degradability. Very recently, owing to the increasing requirements of sustainable development and continuous environmental awareness,[15,16] the search for low-cost and renewable magnetic composites with high removal capacity has become a challenge.

[a]*Institute of Chemical Industry of Forest Products, Chinese Academy of Forestry, National Engineering Lab. for Biomass Chemical Utilization, Key Lab. of Chemical Engineering of Forest Products, National Forestry and Grassland Administration, Key Lab. of Biomass Energy and Material, Nanjing 210042, Jiangsu Province, China. E-mail: envis@163.com; kongzwlhs@163.com*

[b]*Jiangsu Co-Innovation Center of Efficient Processing and Utilization of Forest Resources, Nanjing Forestry University, Nanjing 210037, China*

† Electronic supplementary information (ESI) available. See DOI: 10.1039/d1ra06774e

Lignin is the second most abundant biopolymer and the main renewable aromatic resource on the earth.[17,18] Despite this, lignin has been generated as a byproduct from the pulping industry for a long time and is mainly used in low-value applications like incineration.[19,20] The abundant hydroxyl, methoxy and phenyl groups in the lignin structure,[21] which provide active adsorption sites for adsorption of Pb(II), as well as its low cost, environmental friendliness and biocompatibility,[22] have made lignin an ideal candidate for the preparation of biodegradable composites.[23] Meanwhile, the introduction of lignin significantly enhances the dispersion of Fe_3O_4.[24] Based on the advantages mentioned above, some lignin-based magnetic adsorbents have been successfully synthesized and applied for removing lead pollutants from wastewater.[24,25] Although the developed biobased magnetic adsorbents have overcome the low dispersibility and instability in the heavy metal adsorption process, a facile preparation of a lignin-based magnetic adsorbent with high adsorption efficiency, high adsorption selectivity, fast separation rate and easy recovery from the system is still interesting for wastewater purification.

In this study, we report a novel nanocomposite, L@MNP, obtained by modifying alkenyl lignin onto sulfhydryl magnetic Fe_3O_4 nanoparticles through a thiol–ene click reaction under UV light irradiation. The light-triggered click reactions can be achieved in a rapid and precise manner under mild conditions, and they have been applied in many fields, including biological, material, and environmental sciences.[26,27] Moreover, on the one hand, the magnetic Fe_3O_4 nanoparticles are used as magnetic cores which can be coated with a lignin layer to enhance their chemical stability and avoid self-aggregation and rapid oxidation under the adsorption conditions. On the other hand, owing to the unique characteristics of the thiol–ene click reaction, the alkenyl groups can effectively and selectively react with the thiol groups, which may enable a controllable architecture.[28,29] In addition, the generated thioether groups were expected to provide more adsorption sites for Pb(II) adsorption. The structure and morphology of L@MNP were comprehensively characterized, and the adsorption performance of Pb(II) ions was investigated under different pH values, contact times, initial Pb(II) concentrations, temperatures and co-existing ions, affording insights into the adsorption kinetics, isotherms and thermodynamics. The adsorption mechanism of L@MNP on Pb(II) was also explored.

2. Experimental section

2.1 Materials and chemicals

Lignin was obtained from bamboo feedstock based on acetic acid treatment, and the total content of hydroxyl groups (–OH) was determined to be 2.9 mmol g^{-1} through quantitative ^{31}P NMR spectroscopy. Magnetic Fe_3O_4 nanoparticles (Fe_3O_4 MNPs) with an average particle size of about 30 nm were supplied by Shanghai Aladdin Corporation (China). 3-Bromopropene (99%), sodium hydroxide (NaOH, ≥96%), tetrahydrofuran (THF, ≥99%), ethanol (≥99.7%), tetraethyl orthosilicate (TEOS, SiO_2 ≥28.4%), 3-mercaptopropyl trimethoxysilane (MPTS, 95%), 2,2-bis(hydroxymethyl)propionic acid (DMPA, 99%), and ammonium hydroxide (25–28%) were supplied by Shanghai Adamas Corporation (China). All reagents were of AR grade and were used as received without further purification. Metal ion solutions were obtained from lead nitrate ($Pb(NO_3)_2$, 99%), copper nitrate trihydrate ($Cu(NO_3)_2 \cdot 3H_2O$, 99%), cadmium nitrate tetrahydrate ($Cd(NO_3)_2 \cdot 4H_2O$, 99%), nickel nitrate hexahydrate ($Ni(NO_3)_2 \cdot 6H_2O$, 99%), and zinc nitrate hexahydrate ($Zn(NO_3)_2 \cdot 6H_2O$, 99%) with deionized water.

2.2 Synthesis of sulfhydryl magnetic nanoparticles (SMNP)

Fe_3O_4 MNPs (2.4 g) were dispersed in 800 mL ethanol solution with sonication for over 20 min; then, ammonium hydroxide (8 mL) was added, and sonication proceeded for over 30 min. Then, TEOS (8 mL) was slowly added, and the mixture was continuously stirred at 25 °C for 8 h. The silicon-coated SiO_2@MNPs were collected with a magnet, washed with ethanol and deionized water several times and dried at 70 °C over 12 h.

SiO_2@MNPs (1.8 g) was dispersed in 600 mL of ethanol under sonication for 20 min; then, MPTS (6 mL) was added to the solution, and it was stirred for 12 h. The product sulfhydryl magnetic nanoparticles (SMNP) were washed with ethanol and deionized water several times and collected after drying at 70 °C for 12 h.

2.3 Synthesis of lignin-based magnetic nanoparticles (L@MNP)

Alkenyl lignin (2.6 mmol g^{-1} alkenyl groups) was prepared according to our previous work.[30] For the synthesis of L@MNP: 0.14 g AL (0.37 mmol alkenyl groups) was dissolved in 10 mL THF solution; then, DMPA (96 mg) and SMNP (0.8 g, 0.243 mmol thiol groups) were added to the solution, and the mixture was irradiated under a Hg lamp (365 nm, 2 sun) within a certain time (30 min, 60 min, 90 min). The product was washed with THF and ethanol several times and was subsequently freeze dried to afford L@MNP as a brown powder.

2.4 Characterization

The content of hydroxyl groups of lignin was analyzed by ^{31}P NMR spectroscopy using 2-chloro-4,4,5,5-tetramethyl-1,2,3-dioxaphospholane as a phosphorylating reagent on a Bruker AVANCE III HD 400 MHz NMR spectrometer. A PerkinElmer-2400 analyzer was used to measure the elemental contents of the obtained samples. The functional groups of the samples were characterized in attenuated total reflection (ATR) mode with a resolution of 4 cm^{-1}, enabling measurements ranging from 4000 to 400 cm^{-1} by Fourier transform infrared (FT-IR) spectroscopy on a Nicolet iS50 instrument. The surfaces and microstructures of SMNP and L@MNP were characterized using a Hitachi S3400N scanning electron microscope (SEM) and a JEOL JEM2100F transmission electron microscope (TEM). The surface elements of the prepared samples were also evaluated on the basis of X-ray photoelectron spectroscopy (AXIS-ULTRA DLD, Shimadzu/KRATOS). A VSM7307 vibrating sample

magnetometer (VSM, Lakeshore Corporation) was applied to investigate the magnetic properties of the prepared composites. The crystalline phases of the materials were analyzed with a Bruker D8 Advance diffractometer over an angular range of 10–90° using the X-ray diffraction method.

2.5 Adsorption measurements

Batch experiments were carried out to investigate the Pb(II) adsorption capacity on L@MNP, and the specific operation was as follows: 10 mg adsorbent was added to a 50 mL flask containing 25 mL Pb(II) aqueous solution at a certain concentration, and the flask was placed in a constant temperature oscillator that was set at a rotation speed of 200 rpm. The adsorbent after sufficient adsorption was separated by a 0.22 μm membrane, and the Pb(II) concentration of the residual solution was determined by an inductively coupled plasma atomic emission spectroscopy instrument (ICP, Optima 8000) from PerkinElmer Corp. (US). The adsorption capacity of L@MNP toward heavy metal ions was calculated using eqn (1):[31]

$$q_e = \frac{(C_0 - C_e)V}{m} \quad (1)$$

where q_e (mg g^{-1}) is the adsorption amount of metal ions on L@MNP at equilibrium; C_0 (mg L^{-1}) and C_e (mg L^{-1}) are the initial concentration and the equilibrium concentration of the metal ions, respectively; V (L) is the volume of the solution; and m (g) is the dosage of the adsorbent.

The relative selectivity of L@MNP towards Pb(II), Cu(II), Cd(II), Ni(II) and Zn(II) ions in mixed solution was investigated. Each ion concentration in the mixed solution was the same (C_0 = 200 mg L^{-1}). The distribution coefficient (k) value of each ion was assessed using eqn (2):

$$k = \frac{q_x}{q'} \quad (2)$$

where q_x and q' stand for the adsorption amount of an ion on L@MNP and the total adsorption amount of the other ions in the solution, respectively.

The pH of the initial metal ion solution was adjusted between 2.0 and 6.0 using 0.1 M HCl and 0.1 M NaOH solution. The initial concentration of Pb(II) was 200 mg L^{-1}, and the suspensions were shaken for 180 min at 298 K. An adsorption kinetics study was conducted at pH 5.0 at 298 K for a Pb(II) concentration of 200 mg L^{-1}, with varying shaking times between 1 and 180 min. The adsorption isotherms were developed while varying the initial Pb(II) concentration between 25 and 750 mg L^{-1}. To evaluate the influence of temperature on the adsorption, four different temperatures (15 °C, 25 °C, 35 °C, and 45 °C) were studied at pH 5.0.

HCl (0.1 M) solution was used as an eluting agent for the adsorption–desorption experimental study. The adsorbent L@MNP was placed in 0.1 M HCl solution and shaken at 200 rpm for 180 min; then, a magnet was used to separate it from the solution. Next, the adsorbent was washed many times with HCl and deionized water, then dried to a constant weight at 70 °C. After the above procedure, L@MNP was used for the next adsorption–desorption cycle.

3. Results and discussion

3.1 Preparation and characterization of L@MNP

As presented in Scheme 1, the lignin-based magnetic adsorbent (L@MNP) was fabricated from sulfhydryl-functionalized SMNP and alkenyl lignin *via* the thiol–ene click reaction under UV light (365 nm) irradiation.[32] It was expected that the lignin layer coated on the L@MNP surface would enhance the dispersibility and stability of the magnetic core and simultaneously facilitate its adsorption performance due to the generation of thioether bonds (C–S) as adsorbing sites.[33]

FT-IR spectroscopy was conducted to verify the successful synthesis of L@MNP, as illustrated in Fig. 1a. Two bands at 3381 and 538 cm^{-1} corresponded to the O–H and Fe–O groups of the Fe_3O_4 MNPs sample, respectively.[34] For the SMNP sample, a new peak at 985 cm^{-1} assigned to the Si–O asymmetric vibration could be observed, implying that the silicon layer had been successfully coated on the Fe_3O_4 surface.[35] The characteristic peaks of L@MNP at 1597, 1503 and 1227 cm^{-1} were ascribed to the skeletal vibration of aromatic rings, demonstrating the presence of the lignin layer.[36] Meanwhile, the appearance of the thioether bond (C–S) at 1128 cm^{-1} further confirmed the successful crosslinking between lignin and the magnetic nanoparticles.[37] In addition, the reaction process was monitored by FT-IR spectra (Fig. S1†). At different UV light irradiation intervals (0–90 min), the peak intensity of the C–S bond at 1128 cm^{-1} gradually increased and tended to be stable over 60 min, which revealed the complete transformation of the alkenyl groups into thioether bonds. Elemental analysis was investigated to study the changing contents of C, H and S elements in Fe_3O_4 MNPs, SMNP and L@MNP during the reaction process (Table S1†). After modification with sulfhydryl groups, the sulfur content of SMNP significantly increased to 0.973%. Meanwhile, the carbon content of L@MNP (4.96%) was higher than that of SMNP (1.67%) after the incorporation of lignin, confirming the successful introduction of the lignin component. Moreover, the XRD patterns (Fig. 1b) appearing at 30.0° (220), 35.6° (311), 43.2° (400), 53.9° (422), 57.1° (511) and 62.8° (440) corresponding to typical crystalline Fe_3O_4 (ref. 38) were observed for the Fe_3O_4 MNPs, SMNP and L@MNP samples, respectively, indicating that the magnetic cores remained unchanged regardless of the modification processes.

More features of the morphology were characterized by TEM and SEM (Fig. 2). Upon comparison of the SEM images of SMNP (Fig. 2a) and L@MNP (Fig. 2b), a high similarity in their morphologies was discovered, which confirmed that both SMNP and L@MNP showed a uniform spherical morphology. Due to the coating of SiO_2 and lignin layers, L@MNP possessed a larger particle size (about 37 nm) than the unmodified MNPs (about 30 nm). The TEM image (Fig. 2c) of SMNP demonstrated that the magnetic nanoparticles exhibited a core–shell structure. Additionally, this core–shell structure was maintained for L@MNP (Fig. 2d) with the modification of the lignin layer onto the SMNP surface.[39] The differences caused by the lignin distribution between SMNP and L@MNP were also supported by the XPS analysis. As displayed in Table S2,† the carbon

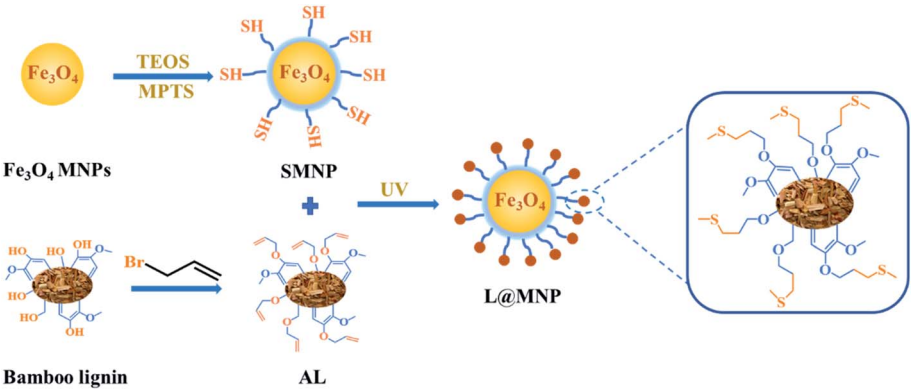

Scheme 1 Synthetic route of L@MNP from bamboo lignin and Fe_3O_4 MNPs.

distribution on SMNP (25.60%) and L@MNP (44.63%) measured by XPS studies was obviously higher than that of SMNP (1.67%) and L@MNP (4.96%) from the elemental analysis, indicating that the lignin component was mainly distributed as a shell layer on the surface of the magnetic Fe_3O_4 core.[25] The surface rate result of S/O in L@MNP was also obtained by XPS and is listed in Table S3.† The results of the porosity characterization (Table S4†) indicated that the surface area and pore structure of L@MNP did not obviously change compared with those of SMNP, which can be attributed to the irregular aggregation of lignin on the SMNP surface.[40]

The magnetic measurement results of the Fe_3O_4 MNPs, SMNP and L@MNP are displayed in Fig. S2.† There was no hysteresis loop in the magnetization curves of SMNP and L@MNP, and both the remanence and coercivity were close to zero; these findings indicated that SMNP and L@MNP were superparamagnetic in nature. The magnetization curves showed that the saturation magnetization of both SMNP (54.46 emu g^{-1}) and L@MNP (51.00 emu g^{-1}) sharply decreased compared to that of the Fe_3O_4 MNPs (84.13 emu g^{-1}) due to the modification of non-magnetic silicon and lignin layers. It is worth mentioning that the saturation magnetization of L@MNP is superior to that of many reported magnetic adsorbents,[33,41] which enables its quick recovery (within 15 s, Fig. S3†) from the aqueous system using an external magnet.

3.2 Adsorption studies

3.2.1 Effect of pH. The effect of the solution pH on the adsorption performance of L@MNP was studied, and the results are shown in Fig. 3a. As the pH value increased from 2.0 to 6.0, the adsorption capacity of L@MNP for Pb(II) increased from 7.25 to 66.25 mg g^{-1}. In the L@MNP structure, both sulphur- and oxygen-containing groups can serve as active sites for chelating Pb(II) ions. When the pH was <5.0, the H_3O^+ species was dominant in solution; thus, only a small amount of cationic Pb(II) ions could be adsorbed, owing to the mutually exclusive force between the protonated surface of L@MNP and the Pb(II) cations. On the other hand, when the pH was >5.0, the H_3O^+ concentration was reduced and the Pb(II) ions were easily coordinated by the adsorbent, which resulted in the rising adsorption capacity of L@MNP.[42] In the case of lead, $Pb(OH)_2$ precipitation began to form at pH > 6.0.[43] Therefore, the solution pH value was set at 5.0 for further adsorption experiments.

3.2.2 Effect of adsorption time. To assess the adsorption process of Pb(II) on L@MNP, the effect of contact time was investigated with the initial Pb(II) concentration set as

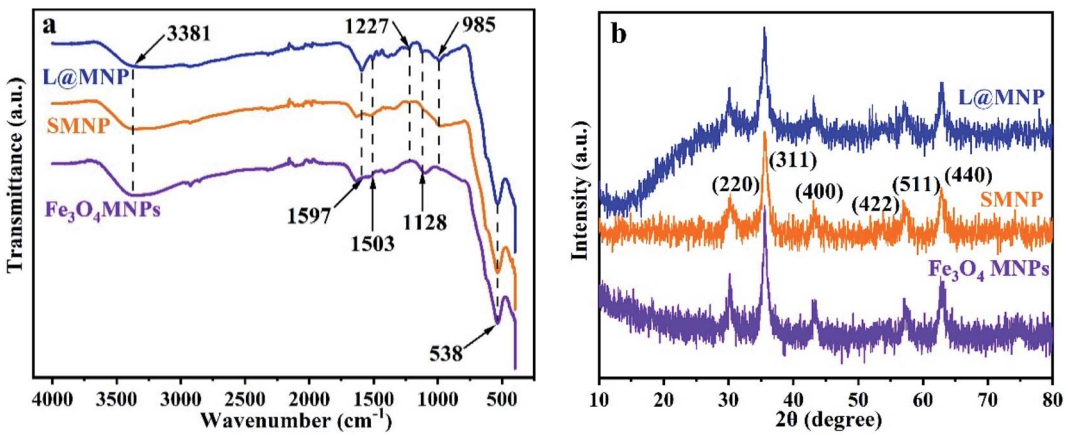

Fig. 1 (a) FT-IR spectra of Fe_3O_4 MNPs, SMNP and L@MNP; (b) XRD patterns of Fe_3O_4 MNPs, SMNP, and L@MNP.

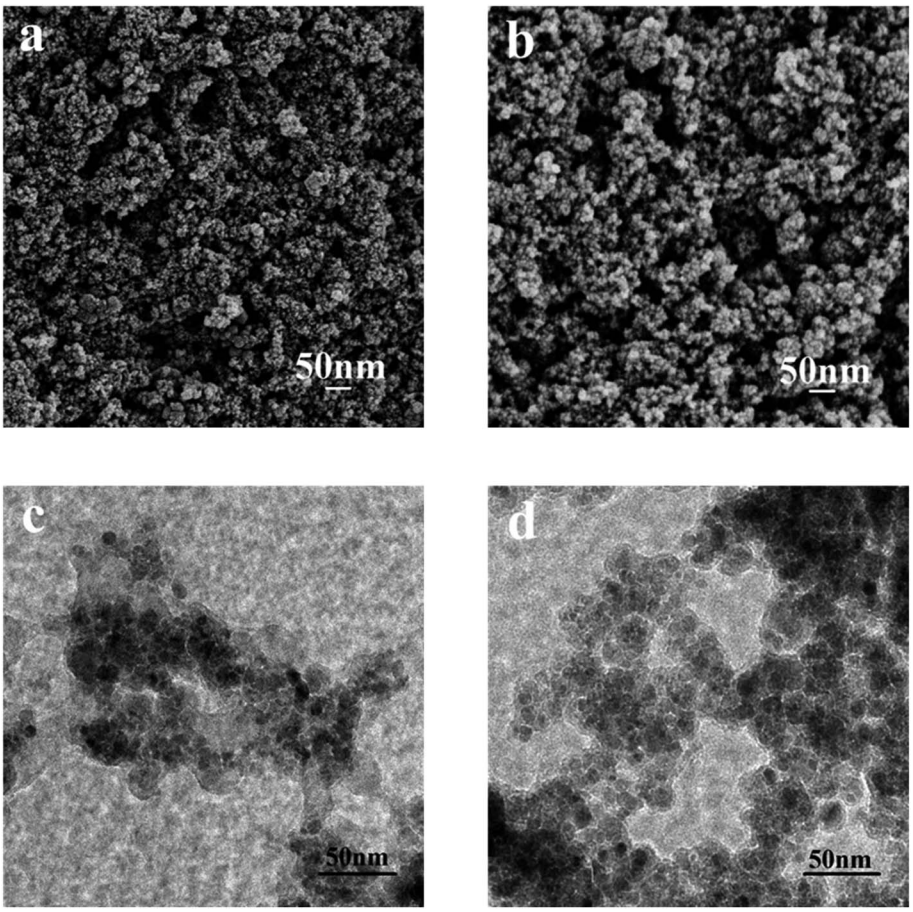

Fig. 2 SEM images of (a) SMNP and (b) L@MNP; TEM images of (c) SMNP and (d) L@MNP.

200 mg L^{-1} at 25 °C. As illustrated in Fig. 3b, the Pb(II) adsorption capacity of L@MNP sharply increased at the initial stage and reached equilibrium (q_e = 64.25 mg g^{-1}) within 30 min. This rapid adsorption of Pb(II) by L@MNP could be mainly attributed to its good dispersion properties within the crosslinked core–shell structure, which was beneficial for ion transportation and provided sufficient binding sites to capture Pb(II).

The obtained kinetics data was fitted by the pseudo-first-order model (eqn (3)), pseudo-second-order model (eqn (4)) and intraparticle diffusion model (eqn (5)) to evaluate the relationship between the adsorption rate and capturing mechanism, respectively,[44] and the fitting results are presented in Fig. 3c and d:

$$\log(q_e - q_t) = \log q_e - \frac{k_1}{2.303}t \quad (3)$$

$$\frac{t}{q_t} = \frac{1}{k_2 q_e^2} + \frac{t}{q_e} \quad (4)$$

$$q_t = k_p t^{0.5} + C \quad (5)$$

where q_e (mg g^{-1}) and q_t (mg g^{-1}) are the Pb(II) adsorption capacity at equilibrium time and time t, respectively, k_1 (min^{-1}) is the pseudo-first-order adsorption kinetic constant, k_2 [g mg^{-1} min^{-1}] is the pseudo-second-order adsorption kinetic constant, k_p [g mg^{-1} $min^{-0.5}$] is the intraparticle diffusion rate constant, and C is a constant.

As displayed in Table 1, the fitting results exhibited that the coefficient (R^2 = 0.9987) of the pseudo-second-order kinetic model was higher than that of the pseudo-first-order kinetic model (R^2 = 0.7805). In addition, the theoretical adsorption capacity (63.13 mg g^{-1}) derived from the pseudo-second-order kinetic model was much closer to the experimental value (62.25 mg g^{-1}), which indicated that the pseudo-second-order kinetic model could well describe the adsorption process. These observations verified that the chemical adsorption played a major role during the adsorption process.[45]

The fitting results of the intraparticle diffusion model showed that there were three stages in the diffusion of Pb(II) onto the adsorbent. Thus, three intraparticle constants (k_{p1}, k_{p2} and k_{p3}) were used to express the diffusion rates of these three stages. It could be found from the fitting data in Table 1 that the diffusion rates followed the order of $k_{p1} > k_{p2} > k_{p3}$. Evidently, the first stage was dominated by rapid surface diffusion in the initial adsorption process (k_{p1} = 15.8078), where a large number of Pb(II) ions were rapidly chelated onto the L@MNP surface.[46] When the surface sites of adsorbent reached saturation, Pb(II)

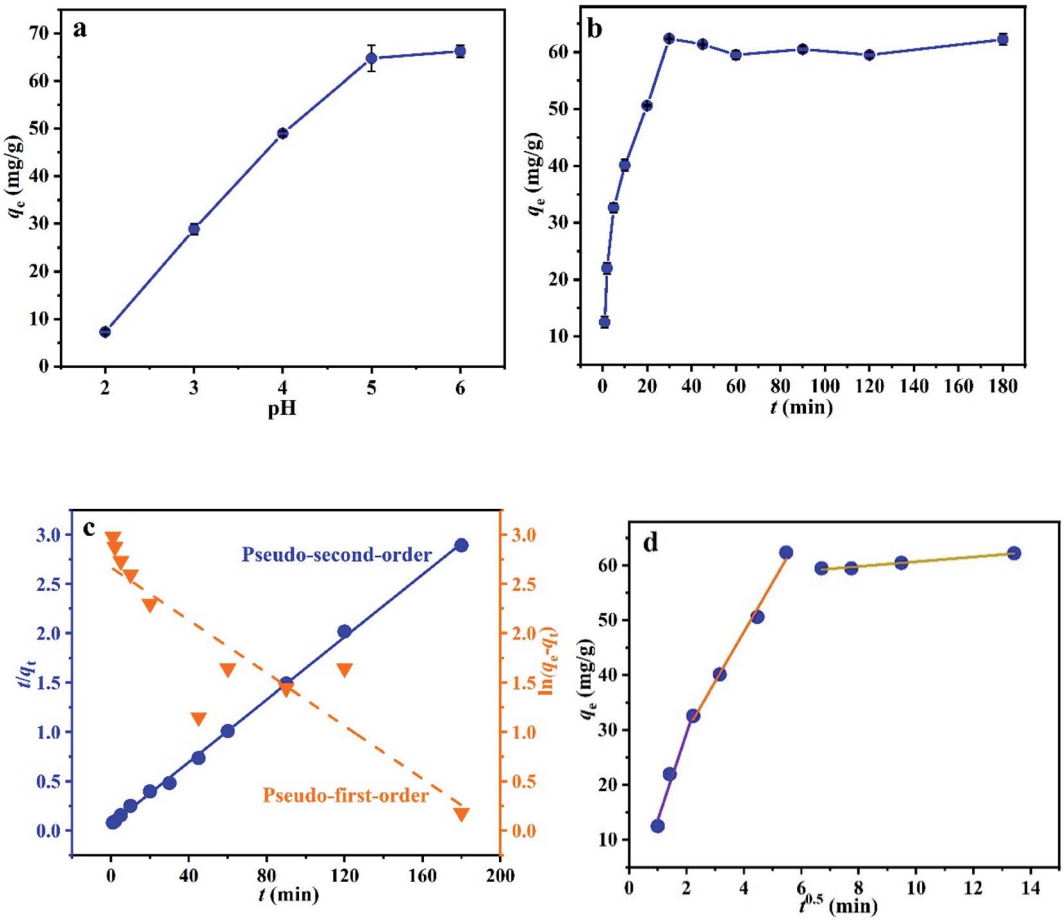

Fig. 3 Effect of (a) pH and (b) contact time on Pb(II) adsorption on L@MNP; adsorption kinetics of Pb(II) on L@MNP by the (c) pseudo-first-order and pseudo-second-order models and (d) intraparticle diffusion model.

Table 1 Kinetic adsorption parameters for Pb(II) adsorption on L@MNP

Pseudo-first-order model					
q_e (mg g^{-1})		k_1 (min^{-1})		R^2	
25.87		0.02871		0.7805	
Pseudo-second-order model					
q_e (mg g^{-1})		k_2 [g mg^{-1} min^{-1}]		R^2	
63.13		0.00414		0.9987	
Intraparticle diffusion model					
k_{p1} [g mg^{-1} min$^{-0.5}$]	R_1^2	k_{p2} [g mg^{-1} min$^{-0.5}$]	R_2^2	k_{p3} [g mg^{-1} min$^{-0.5}$]	R_3^2
15.8078	0.9518	9.0273	0.9877	0.4351	0.9794

ions began to diffuse into the pores of the adsorbent and attached to the inner surface during the second stage. At the same time, resistance occurred when Pb(II) diffused into the adsorbent pores, which led to the decrease of the diffusion rate constant (k_{p2} = 9.0273).[47] Subsequently, the third stage represented the adsorption equilibrium stage. As diffusion continued, the active sites on the inner surface of the adsorbent for the most part had reached adsorption equilibrium, which led to the minimum diffusion rate constant (k_{p3} = 0.4351) in three stages.[48] In addition, because the fitting line did not pass through the zero point, it seemed that boundary diffusion and external diffusion would also affect the Pb(II) adsorption process on L@MNP.

3.2.3 Adsorption isotherms. The adsorption isotherms of L@MNP for Pb(II) were studied at various initial Pb(II) concentrations (25–750 mg L^{-1}), pH 5.0, and 25 °C. As displayed in Fig. 4a, the adsorption capacity of L@MNP increased with ascending initial Pb(II) concentration. The adsorption behavior of L@MNP was analyzed using the Langmuir model (eqn (6))[49] and Freundlich model (eqn (7)),[50] respectively:

$$q_e = \frac{K_L q_{max} C_e}{1 + K_L C_e} \quad (6)$$

$$q_e = K_F C_e^{1/n} \quad (7)$$

where q_e (mg g^{-1}) is the adsorption capacity at equilibrium, q_{max} (mg g^{-1}) is the maximum adsorption capacity of L@MNP, C_e

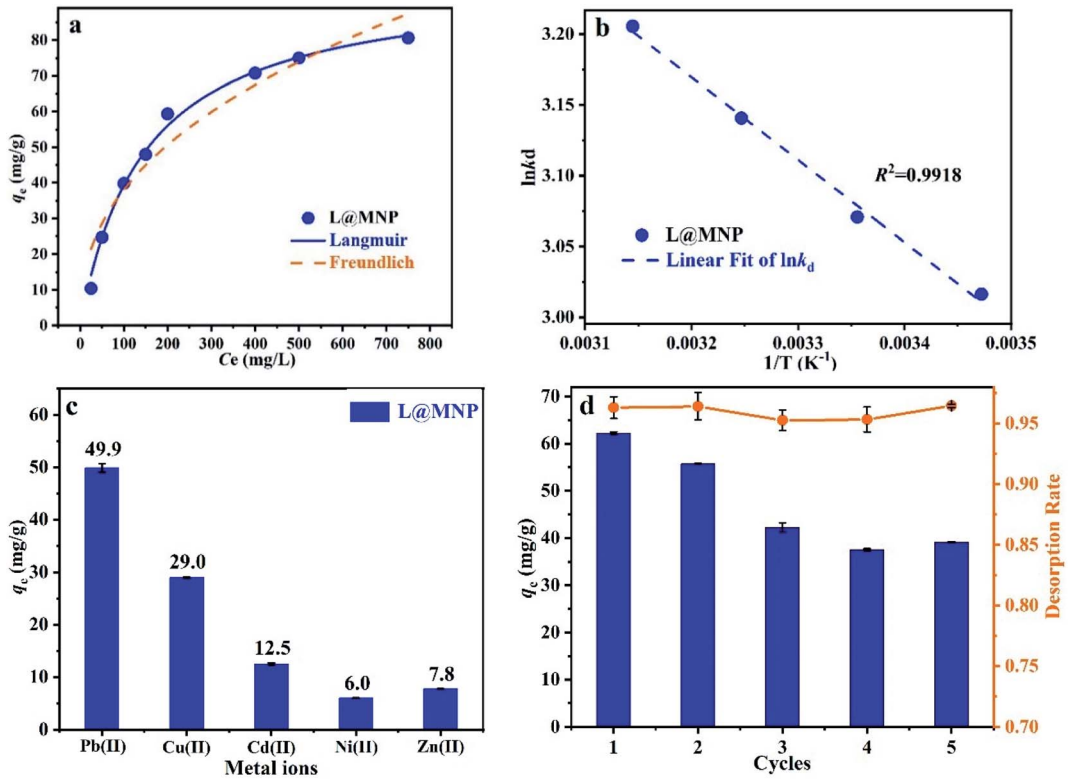

Fig. 4 (a) Equilibrium data and fitting curves for Pb(II) adsorption on L@MNP; (b) plot of $1/T$ *versus* ln k_d of L@MNP; (c) adsorption selectivity of L@MNP for co-existing metal ions; (d) adsorption–desorption cycles of L@MNP for Pb(II) recovery (pH 5.0, dosage 10 mg/25 mL, 200 mg L^{-1} Pb(II) solution, 25 °C, and 180 min).

(mg L^{-1}) is the solution concentration at adsorption equilibrium, K_L (L mg^{-1}) is the Langmuir model constant, K_F (mg g^{-1}) is the Freundlich model constant, and $1/n$ is the Freundlich adsorption coefficient.

The fitting curves and parameters of the Langmuir and Freundlich models are shown in Fig. 4a and Table 2, respectively. These fitting findings indicated that the adsorption of Pb(II) by L@MNP closely followed the Langmuir model with a high fitting coefficient (R^2 = 0.9928), demonstrating a monolayer adsorption process.[51] In addition, q_{max} was calculated to be 97.38 mg g^{-1}, which was not only obviously higher than that of the raw lignin (q_{max} = 12.00 mg g^{-1}), but also surpassed that of many reported adsorbents (Table 3).

Table 2 Fitting parameters of the Langmuir and Freundlich models for Pb(II)

Langmuir isotherm model		
Q_{max} (mg g^{-1})	K_L (min^{-1})	R^2
97.38	0.00678	0.9928
Freundlich isotherm model		
K_F	$1/n$	R^2
5.6791	0.4130	0.9244

3.2.4 Adsorption thermodynamics. The adsorption thermodynamics were further investigated to explore the energy changes and feasibility of Pb(II) adsorption on L@MNP at temperatures ranging from 25 °C to 45 °C. Correspondingly, the thermodynamic parameters, including the Gibbs free energy change (ΔG^0, kJ mol^{-1}), enthalpy change (ΔH^0, kJ mol^{-1}), and entropy change [ΔS^0, J mol^{-1} K^{-1}], could be calculated based on eqn (8)–(10):[61]

$$\Delta G^0 = -RT \ln k_d \quad (8)$$

$$\ln k_d = -\frac{\Delta H^0}{RT} + \frac{\Delta S^0}{R} \quad (9)$$

$$k_d = \frac{q_e}{C_e} \quad (10)$$

where R [8.314 J mol^{-1} K^{-1}] stands for the universal gas constant and k_d is the distribution coefficient.

The linear function of ln k_d *versus* $1/T$ was fitted based on the equilibrium adsorption data at different adsorption temperatures (Fig. 4b), and the thermodynamic parameters are shown in Table 4. Negative values of ΔG^0 at all tested temperatures implied that the adsorption process occurred spontaneously.[62] Meanwhile, the ΔG^0 values decreased gradually with the increase of temperature, indicating that the driving force in the

Table 3 Adsorption capacities of different adsorbents reported for Pb(II)

Adsorbents	Condition		q_{max} (mg g^{-1})	Ref.
	pH	Temperature (K)		
Lignin	—[a]	330	9.00	52
1-Aza-18-crown-6 functionalized lignin-based adsorbent (AFL)	6.0	298	91.4	53
Lignin xanthate resin	5.0	303	63.90	54
Waste biomass	5.0	298	160.00	55
Nitrilotriacetic acid anhydride modified ligno-cellulosic material (NTAA-LCM)	3.8	298	303.52	56
N-Acetyl-L-cysteine-functionalized lignin (CFL)	6.0	288	58.80	31
Thiol-functionalized cellulose nanofiber membrane	4.0	rt[b]	22.00	57
Magnetized activated carbons (MAC)	5.0	298	253.20	58
Lignin derivate magnetic hydrogel microspheres	5.0	298	33.00	59
Magnesium oxide cores with silica coated nano-magnetite (MTM)	—[a]	298	85.10	60
L@MNP	5.0	298	97.38	This study
Raw lignin	5.0	298	12.00	This study

[a] Not available. [b] Room temperature.

Table 4 Parameters of thermodynamic adsorption for Pb(II) on L@MNP

Adsorbent	ΔH^0 (kJ mol^{-1})	ΔS^0 [J K^{-1} mol^{-1}]	ΔG^0 (kJ mol^{-1})			
			298 K	308 K	318 K	328 K
L@MNP	6.36	46.80	−7.12	−7.58	−8.05	−8.52

adsorption was positively correlated with the spontaneous degree range.[63] The positive value of ΔH^0 proved that the adsorption was endothermic in nature. Additionally, the positive value of ΔS^0 suggested an increasing freedom degree at the solid–liquid interface.[64]

3.2.5 Adsorption selectivity. It is impossible for actual sewage to contain only a single heavy metal. Thus, different co-existing substances, including Cu(II), Cd(II), Ni(II) and Zn(II) ions, were tested herein for possible competitive effects on the adsorption of Pb(II) by L@MNP at pH 5.0 and 25 °C. As presented in Fig. 4c, the adsorption capacities of L@MNP toward various heavy metal ions were found to follow the order of Pb(II) > Cu(II) > Cd(II) > Zn(II) > Ni(II). Despite suffering electrostatic repulsion among various cations,[65] L@MNP still showed excellent selectivity toward Pb(II) over other competitive metal ions. Concurrently, the affinity and selectivity of L@MNP to various metal cations could be distinguished *via* comparing the distribution coefficients (k). As listed in Table 5, the high relative k (0.903) for Pb(II) enables L@MNP to function as an excellent selective adsorbent for Pb(II) adsorption. On the basis of Pearson's hard/soft acid/base (HSAB) theory, Pb(II) has been classified as a softer acid than other metal ions due to its higher water binding energy and larger radius of hydrated ions. Thus, the S/O-containing functional groups serving as soft bases in L@MNP could feasibly chelate the soft metal Pb(II),[66] which results in remarkable selectivity for Pb(II) capture.

Table 5 Adsorption selectivity parameters of L@MNP for metal ions

Adsorbent	Selective coefficient k				
	k (Pb)	k (Cd)	k (Cu)	k (Ni)	k (Zn)
L@MNP	0.903	0.381	0.135	0.061	0.080

3.2.6 Adsorption recyclability. The recyclability characteristics of an adsorbent are critical in its practical application. Under suitable adsorption conditions (pH 5.0, T = 25 °C and contact time 180 min), the Pb(II)-loaded L@MNP could be desorbed by rinsing with 0.1 M HCl solvent to evaluate its reusability performance. As shown in Fig. 4d, the adsorption efficiency remained at 62.86% after 5 adsorption–desorption cycles. Additionally, the desorption efficiency of L@MNP was found to be over 95.27%. Thus, the acceptable regeneration performance of L@MNP would favor recyclable utilization in wastewater treatment.

3.2.7 Adsorption mechanism. For the purpose of proving the adsorption mechanism between the adsorbent and metal ion pollutants, the L@MNP samples before and after Pb(II) adsorption were detected by XPS spectra (Fig. 5a–c). As shown in Fig. 5a, the high-resolution XPS spectrum showed three characteristic peaks of Pb $4f_{3/2}$, Pb $4f_{5/2}$ Pb $4f_{7/2}$ at 436.3, 414.4 and 139.5 eV, respectively, which indicated that Pb(II) was adsorbed onto the L@MNP surface in an ionic state.[67] Fig. 5b and c present the obvious shifts of the O 1s and S 2p peaks, which proved that both O and S-containing groups contributed to the adsorption process. Particularly, three O 1s peaks at 532.8, 530.8, and 529.7 eV, attributed to Si–O, C–O and Fe–O groups, moved to 532.9, 531.5 and 530.1 eV after Pb(II) was adsorbed onto the L@MNP surface, respectively.[68] Meanwhile, two S 2p peaks at 164.8 and 162.9 eV, ascribed to the C–S and –SH groups of L@MNP, shifted to 167.9 and 163.5 eV for L@MNP-Pb(II), respectively; this confirms that the coordination behavior also occurred between sulfur-containing groups and Pb(II).[69–71] These observations could be explained as follows: after Pb(II) adsorption, O and S atoms

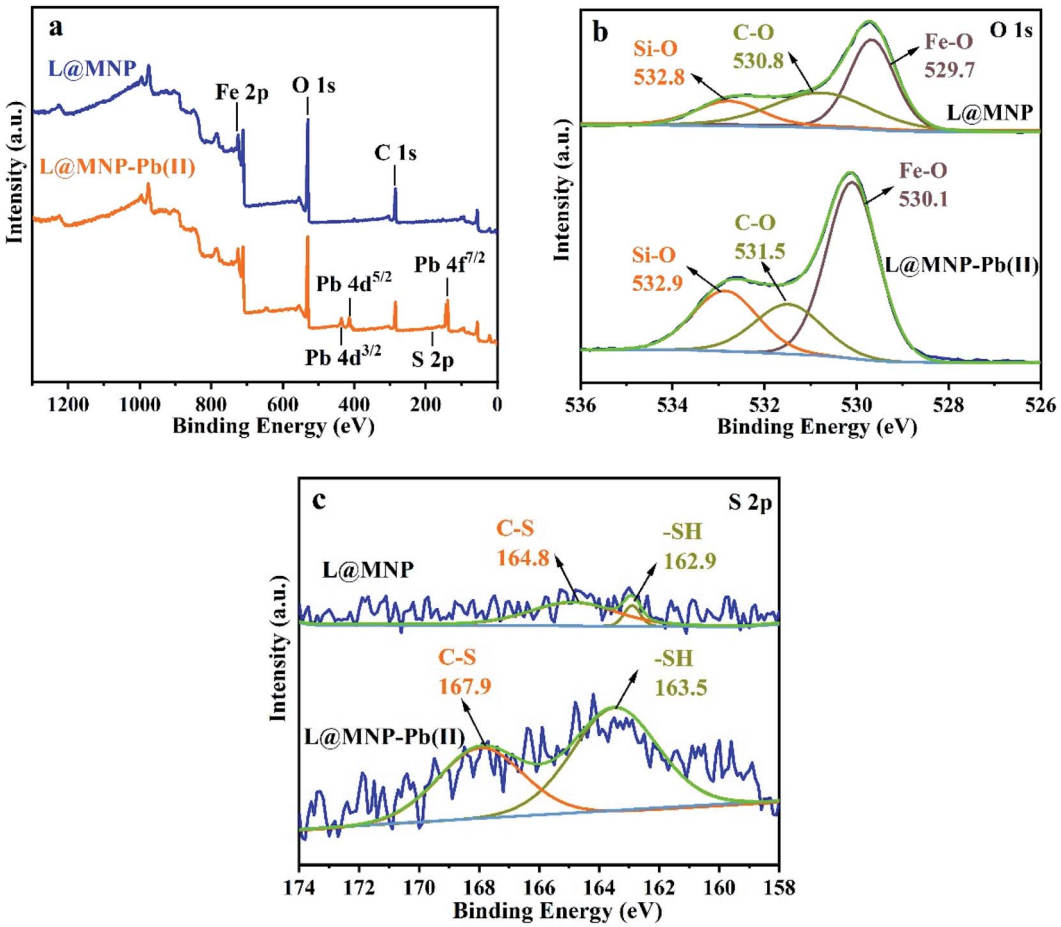

Fig. 5 (a) XPS survey spectra, (b) O 1s and (c) S 2p spectra of L@MNP before and after Pb(II) adsorption.

shared lone pair electrons with the adsorbed Pb(II), which caused them to shift to a higher binding energy with the decreased electron density.[37] Based on the above findings, the complexation of Pb(II) with functional groups was involved in the primary interaction mechanism between L@MNP and Pb(II) ions.

4. Conclusions

In summary, we have demonstrated a novel lignin-based magnetic adsorbent, L@MNP, that was synthesized through a thiol–ene click reaction. Structural and morphological characterizations were comprehensively investigated to gain detailed insight into L@MNP. The Pb(II) adsorption on L@MNP closely followed the pseudo-second-order kinetic model and the Langmuir isothermal model, yielding a rapid adsorption equilibrium (within 30 min) and a relatively high q_{max} of 97.38 mg g^{-1}. Thermodynamic adsorption investigations indicated a spontaneous and exothermic process. In addition, L@MNP exhibited excellent selectivity and acceptable reusability for Pb(II) adsorption, with fast recovery behavior. We anticipate that the present findings will offer a novel strategy for the development of lignin-based adsorbent materials for wastewater treatment.

Conflicts of interest

There are no conflicts to declare.

Acknowledgements

We greatly acknowledge support from the National Key Research and Development Program of China (2017YFE0106800), Fundamental Research Funds of CAF (CAFYBB2019QB008), National Natural Science Foundation of China (31971615), and Fundamental Research Funds of Jiangsu Key Laboratory of Biomass Energy and Material (JSBEM-S-201806).

References

1 S. Bolisetty, M. Peydayesh and R. Mezzenga, *Chem. Soc. Rev.*, 2019, **48**, 463–487.
2 R. Zhang, T. Chen, Y. Zhang, Y. Hou and Q. Chang, *Chemosphere*, 2020, **252**, 126591.
3 K. Renu, R. Chakraborty, H. Myakala, R. Koti, A. C. Famurewa, H. Madhyastha, B. Vellingiri, A. George and A. Valsala Gopalakrishnan, *Chemosphere*, 2021, **271**, 129735.

4 J. Verma, S. Kumari and A. Dhasmana, *Int. J. Innov. Res. Technol.*, 2020, **7**, 672–676.
5 M. Naushad, T. Ahamad and K. M. Al-sheetan, *J. Hazard. Mater.*, 2021, **407**, 124816.
6 M. Hasanpour and M. Hatami, *Adv. Colloid Interface Sci.*, 2020, **284**, 102247.
7 L. P. Zhang, Z. Liu, X. L. Zhou, C. Zhang, Q. W. Cai, R. Xie, X. J. Ju, W. Wang, Y. Faraj and L. Y. Chu, *Sep. Purif. Technol.*, 2020, **237**, 116364.
8 Q. T. Zhang, M. F. Li, B. Luo, Y. Y. Luo, H. R. Jiang, C. Z. Chen, S. F. Wang and D. Y. Min, *J. Hazard. Mater.*, 2021, **402**, 123445.
9 M. L. Mao, T. T. Yan, J. J. Shen, J. P. Zhang and D. S. Zhang, *Environ. Sci. Technol.*, 2021, **55**, 3333–3340.
10 C. F. Carolin, P. S. Kumar, A. Saravanan, G. J. Joshiba and M. Naushad, *J. Environ. Chem. Eng.*, 2017, **5**, 2782–2799.
11 W. S. Chai, J. Y. Cheun, P. S. Kumar, M. Mubashir, Z. Majeed, F. Banat, S.-H. Ho and P. L. Show, *J. Cleaner Prod.*, 2021, **296**, 126589.
12 F. F. Gao, *ChemistrySelect*, 2019, **4**, 6805–6811.
13 K. K. Chenab, B. Sohrabi, A. Jafari and S. Ramakrishna, *Mater. Today Chem.*, 2020, **16**, 100262.
14 F. Almomani, R. Bhosale, M. Khraisheh, A. kumar and T. Almomani, *Appl. Surf. Sci.*, 2020, **506**, 144924.
15 X. Q. Lin, Y. Liu, X. J. Zheng and N. Qureshi, *Ind. Crops Prod.*, 2021, **162**, 113258.
16 H. Y. Liu, H. S. Du, T. Zheng, K. Liu, X. X. Ji, T. Xu, X. Y. Zhang and C. L. Si, *Chem. Eng. J.*, 2021, **426**, 130817.
17 Y. Wu, Y. Qian, H. M. Lou, D. J. Yang and X. Q. Qiu, *ACS Sustainable Chem. Eng.*, 2019, **7**, 15966–15973.
18 J. Y. Xu, C. Y. Li, L. Dai, C. L. Xu, Y. D. Zhong, F. X. Yu and C. L. Si, *ChemSusChem*, 2020, **13**, 4284–4295.
19 W. J. Gao and P. Fatehi, *Can. J. Chem. Eng.*, 2019, **97**, 2827–2842.
20 N. Supanchaiyamat, K. Jetsrisuparb, J. T. N. Knijnenburg, D. C. W. Tsang and A. J. Hunt, *Bioresour. Technol.*, 2019, **272**, 570–581.
21 J. Ralph, C. Lapierre and W. Boerjan, *Curr. Opin. Biotechnol.*, 2019, **56**, 240–249.
22 J. Y. Wang, Y. Qian, L. B. Li and X. Q. Qiu, *ChemSusChem*, 2020, **13**, 4420–4427.
23 Y. L. Liu, C. Jin, Z. Z. Yang, G. M. Wu, G. F. Liu and Z. W. Kong, *Int. J. Biol. Macromol.*, 2021, **187**, 880–891.
24 Y. C. Zhang, S. Z. Ni, X. J. Wang, W. H. Zhang, L. Lagerquist, M. H. Qin, S. Willför, C. L. Xu and P. Fatehi, *Chem. Eng. J.*, 2019, **372**, 82–91.
25 X. Zhou, C. Jin, G. F. Liu, G. M. Wu, S. P. Huo and Z. W. Kong, *Chem. Eng. J.*, 2021, **420**, 130409.
26 G. S. Kumar and Q. Lin, *Chem. Rev.*, 2021, **121**, 6991–7031.
27 X. Y. Ji, Z. X. Pan, B. C. Yu, L. K. D. L. Cruz, Y. Q. Zheng, B. W. Ke and B. H. Wang, *Chem. Soc. Rev.*, 2019, **48**, 1077.
28 C. Jin, X. Y. Zhang, J. N. Xin, G. F. Liu, G. M. Wu, Z. W. Kong and J. W. Zhang, *ACS Sustainable Chem. Eng.*, 2017, **5**, 4086–4093.
29 P. L. Yap, S. Kabiri, D. N. H. Tran and D. Losic, *ACS Appl. Mater. Interfaces*, 2019, **11**, 6350–6362.
30 C. Jin, X. Y. Zhang, J. N. Xin, G. F. Liu, J. Chen, G. M. Wu, T. Liu, J. Zhang and Z. Kong, *Ind. Eng. Chem. Res.*, 2018, **57**, 7872–7880.
31 Y. J. Huang, W. C. Zhao, X. Zhang, H. Peng and Y. F. Gong, *Chem. Eng. J.*, 2019, **375**, 121935.
32 X. Wang, H. X. Guo, Z. H. Lu, X. Liu, X. F. Luo, S. J. Li, S. X. Liu, J. Li, Y. Z. Wu and Z. J. Chen, *ACS Appl. Mater. Interfaces*, 2021, **13**, 33536–33545.
33 H. F. He, X. Y. Meng, Q. Y. Yue, W. Y. Yin, Y. Gao, P. Fang and L. Shen, *Chem. Eng. J.*, 2021, **405**, 126743.
34 P. L. Yap, Y. L. Auyoong, K. Hassan, F. Farivar, D. N. H. Tran, J. Ma and D. Losic, *Chem. Eng. J.*, 2020, **395**, 124965.
35 X. Y. Guo, F. F. Mao, W. J. Wang, Y. Yang and Z. M. Bai, *ACS Appl. Mater. Interfaces*, 2015, **7**, 14983–14991.
36 A. N. M. Nasir, N. Yahaya, N. N. M. Zain, V. Lim, S. Kamaruzaman, B. Saad, N. Nishiyama, N. Yoshida and Y. Hirota, *Food Chem.*, 2019, **276**, 458–466.
37 A. Deng, J. Yuan, C. Z. Qi and Y. Gao, *Mater. Chem. Phys.*, 2020, **243**, 122625.
38 Y. Hao, Y. Gao, L. Y. Gao, Y. L. He, Y. Y. Niu, S. Hussain, R. X. Gao, L. D. Pfefferle, M. Shahid and S. C. Wang, *Chem. Eng. J.*, 2021, **423**, 129817.
39 X. Liu, J. N. Guan, H. G. Lai, Q. Xu, X. B. Bai, Z. M. Wang and S. P. Cui, *J. Cleaner Prod.*, 2020, **253**, 119915.
40 B. P. Zhang, D. J. Yang, X. Q. Qiu, Y. Qian, M. Z. Yan and Q. Li, *J. Ind. Eng. Chem.*, 2020, **82**, 220–227.
41 D. K. Cheng, X. H. Dai, L. Chen, Y. H. Cui, C. W. Qiang, Q. Sun and J. D. Dai, *ACS Sustainable Chem. Eng.*, 2019, **8**, 771–781.
42 S. Shahraki, H. S. Delarami, F. Khosravi and R. Nejat, *J. Colloid Interface Sci.*, 2020, **576**, 79–89.
43 H. C. Wang, Z. W. Wang, R. R. Yue, F. Gao, R. L. Ren, J. F. Wei, X. L. Wang and Z. Y. Kong, *Chem. Eng. J.*, 2020, **383**, 123107.
44 Z. H. Duan, W. H. Zhang, M. W. Lu, Z. W. Shao, W. L. Huang, J. Li, Y. N. Li, J. C. Mo, Y. T. Li and C. Y. Chen, *Carbon*, 2020, **167**, 351–363.
45 R. H. Mu, B. Liu, X. Chen, N. Wang and J. Yang, *Int. J. Biol. Macromol.*, 2020, **163**, 120–127.
46 C. L. Jiang, X. H. Wang, B. X. Hou, C. Hao, X. Li and J. B. Wu, *J. Agric. Food Chem.*, 2020, **68**, 3050–3060.
47 Z. J. Wu, W. X. Huang, X. Y. Shan and Z. L. Li, *Int. J. Biol. Macromol.*, 2020, **143**, 325–333.
48 A. Y. Li, H. Deng, Y. H. Jiang, C. H. Ye, B. G. Yu, X. L. Zhou and A. Y. Ma, *Langmuir*, 2020, **36**, 9160–9174.
49 L. Dai, Y. T. Li, R. Liu, C. L. Si and Y. C. Ni, *Int. J. Biol. Macromol.*, 2019, **132**, 478–486.
50 X. F. Zhou, Z. R. Jia, A. L. Feng, S. L. Qu, X. N. Wang, X. H. Liu, B. B. Wang and G. L. Wu, *J. Colloid Interface Sci.*, 2020, **575**, 130–139.
51 M. Bugarčić, Z. Lopičić, T. Šoštarić, A. Marinković, J. D. Rusmirovic, D. Milošević and M. Milivojević, *J. Environ. Chem. Eng.*, 2021, **9**, 106020.
52 A. Demirbas, *J. Hazard. Mater.*, 2004, **109**, 221–226.
53 C. Jin, G. F. Liu, G. M. Wu, S. P. Huo, Z. S. Liu and Z. W. Kong, *Ind. Crops Prod.*, 2020, **155**, 112829.

54 Z. L. Li, Y. Kong and Y. Y. Ge, *Chem. Eng. J.*, 2015, **270**, 229–234.
55 Y. Cheng, C. Yang, H. He, G. Zeng, K. Zhao and Y. Zhou, *J. Environ. Eng.*, 2016, **142**, C4015001.
56 Y. Q. Huang, C. P. Yang, Z. C. Sun, G. M. Zeng and H. J. He, *RSC Adv.*, 2015, **5**, 11475–11484.
57 H. Y. Choi, J. H. Bae, Y. Hasegawa, S. An, I. S. Kim, H. Lee and M. Kim, *Carbohydr. Polym.*, 2020, **234**, 115881.
58 Z. Zhang, T. Wang, H. X. Zhang, Y. H. Liu and B. S. Xing, *Sci. Total Environ.*, 2021, **757**, 143910.
59 Y. Meng, C. X. Li, X. Q. Liu, J. Lu, Y. Cheng, L. P. Xiao and H. S. Wang, *Sci. Total Environ.*, 2019, **685**, 847–855.
60 R. Nagarajah, K. T. Wong, G. Lee, K. H. Chu, Y. Yoon, N. C. Kim and M. Jang, *Sep. Purif. Technol.*, 2017, **174**, 290–300.
61 Y. Liu, P. Qian, Y. Yu, B. Yu, Y. L. Wang, S. F. Ye and Y. F. Chen, *J. Environ. Sci.*, 2018, **67**, 224–236.
62 Q. J. Wang, Y. Zhang, X. X. Wangjin, Y. L. Wang, G. H. Meng and Y. H. Chen, *J. Environ. Sci.*, 2020, **87**, 272–280.
63 H. C. Wang, Z. W. Wang, R. R. Yue, F. Gao, R. L. Ren, J. F. Wei, X. L. Wang and Z. Y. Kong, *J. Hazard. Mater.*, 2020, **384**, 121288.
64 E. Mahmoudi, S. Azizkhani, A. W. Mohammad, L. Y. Ng, A. Benamor, W. L. Ang and M. Ba-Abbad, *J. Environ. Sci.*, 2020, **98**, 151–160.
65 C. K. Liu, R. B. Bai and Q. S. SanLy, *Water Res.*, 2008, **42**, 1511–1522.
66 S. F. Bo, J. M. Luo, Q. D. An, Z. Y. Xiao, H. S. Wang, W. J. Cai, S. R. Zhai and Z. C. Li, *J. Cleaner Prod.*, 2020, **250**, 119585.
67 J. W. Pan, B. Y. Gao, S. Y. Wang, K. Y. Guo, X. Xu and Q. Y. Yue, *Sci. Total Environ.*, 2020, **737**, 140283.
68 J. J. Zhao, L. P. Luan, Z. W. Li, Z. F. Duan, Y. F. Li, S. B. Zheng, Z. X. Xue, W. L. Xu and Y. Z. Niu, *J. Alloys Compd.*, 2020, **825**, 154051.
69 M. F. Yan, W. X. Huang and Z. L. Li, *Int. J. Biol. Macromol.*, 2019, **136**, 927–935.
70 S. B. Zeng, L. G. Li, L. H. Xie, D. K. Zhao, N. Wang and S. W. Chen, *ChemSusChem*, 2017, **10**, 3378–3386.
71 N. Ballav, R. Das, S. Giri, A. M. Muliwa, K. Pillay and A. Maity, *Chem. Eng. J.*, 2018, **345**, 621–630.